ACS OMEGA

Article

Cite This: ACS Omega 2019, 4, 6399−6410

http://pubs.acs.org/journal/acsodf

Green Approach for Synthesizing Three Different Carbon Microstructures from a Single Biowaste *Bombax malabaricum* for Fully Biocompatible Flexible Supercapacitors and Their Performance in Various Electrolytes

Sandhya Rani Mangisetti,[†,‡] M. Kamaraj,[‡] and Ramaprabhu Sundara*[,†]

[†]Alternative Energy and Nanotechnology Laboratory, Department of Physics and [‡]Department of Metallurgical and Materials Engineering, Indian Institute of Technology Madras, Chennai 600036, India

Supporting Information

ABSTRACT: The scalable design and inexpensive synthesis of high-surface-area conductive porous carbon electrode materials for high-performance supercapacitors have found extensive interest. Typically, the inherent structure and composition of the biomass or biowaste influence the final structural and morphological properties of carbon nanomaterials. To investigate the influence of internal microstructure on the final products and their effect on electrochemical performance, herein, for the first time, we demonstrated a facile approach for the synthesis of three unique microstructures. N-doped two-dimensional wrinkled few-layered porous graphene nanosheets (N-HGNSs), three-dimensional honeycomb-like porous carbon (N-HPC), and carbon microflakes (N-CMF) are synthesized from three different parts of a single biowaste material, *Bombax malabaricum*. N-HGNS, N-HPC, and N-CMF electrode materials exhibit high specific capacitance (C_p) values of 523, 458, and 363 F g^{-1}, respectively, at a high current density of 1.5 A g^{-1} in 1 M H_2SO_4 with a high rate capability of ∼82% at 30 A g^{-1}, which are, to the best of our knowledge, among the highest ever testified for N-doped carbon materials obtained from biowaste. Furthermore, a fully biocompatible flexible solid-state supercapacitor device is successfully designed with high energy densities of 19.4 and 17.84 Wh kg^{-1}, as well as excellent energy densities of 76.9 and 53 Wh kg^{-1} are presented in Na_2SO_4 electrolyte for N-HGNS and N-HPC electrodes, respectively. It is believed that this single-step novel green approach could aid in the design of an efficient and large-scale process to prepare electrode materials with tunable properties from biowaste for excellent energy storage applications. Furthermore, the three flexible supercapacitors connected in series can power a red light-emitting diode for 20 and 15 min after charging for 60 s for N-HGNS and N-HPC, respectively.

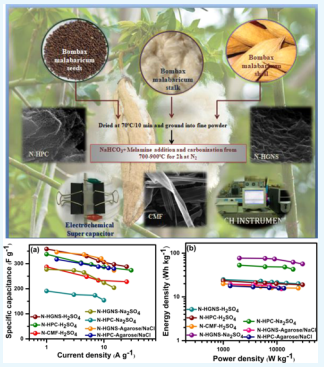

INTRODUCTION

In recent times, electrochemical supercapacitors have attracted considerable attention due to their high power density, long cycle life, and quick charge−discharge rate.[1] Since supercapacitors can deliver high power in short pulses, they have found applications in heavy electric vehicles, power backup systems, and portable electronic devices.[2,3] However, the only limitation associated with the supercapacitors compared with batteries is their lower energy density.[4] Based on the energy storage mechanism, electrochemical supercapacitors are classified into two types. One of them is the electric double-layer capacitor, in which the energy storage takes place at the electrode−electrolyte interface. The other supercapacitor type is the pseudocapacitor, in which the energy storage takes place due to the fast redox reactions of the electroactive materials at the electrode surface. Although pseudomaterials such as metal oxides and conducting polymers exhibit high specific capacitance, their high cost and poor cycle life limit their practical applications.[5] To address these difficulties, carbon nanocomposites are designed along with the pseudomaterials. One of the productive ways of introducing pseudocapacitive behavior is through the incorporation of heteroatoms on the surface of carbon materials. These doped heteroatoms contribute pseudocapacitance, improve the surface wettable properties of the carbon materials, and also alter the electrochemical properties of the carbon nanomaterials.[6] The fabricated supercapacitors utilizing such electrode materials would exhibit the combined electric double layer and pseudocapacitive behavior to obtain relatively high capacitance, long-term cycle stability, and quick charge−discharge. In general, nitrogen-doped carbon nanomaterials are synthesized by either post-treatment of carbon materials with the nitrogen source, i.e., polypyrrole, or doping during carbonization of carbon materials along with nitrogen-rich sources.[7]

In recent times, research and development have concentrated on finding various novel nanomaterials that can find applications in energy storage and conversion devices.[8,9] Although a variety of feasible designs are already presented,

Received: January 29, 2019
Accepted: March 22, 2019
Published: April 8, 2019

DOI: 10.1021/acsomega.9b00263
ACS Omega 2019, 4, 6399−6410

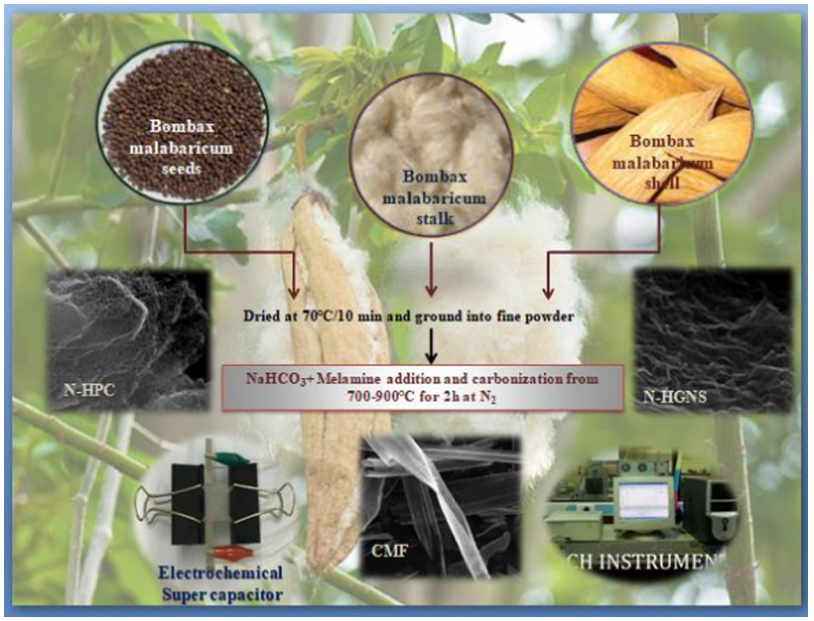

Figure 1. Schematic representation of the synthesis process of N-HGNS, N-CMF, and N-HPC.

the demand of novel materials with a high electrochemical performance that can overcome some challenges, such as the dependency on the abundant and expensive precursors and multiple preparation steps using toxic chemical reagents, is increasing.[10−13] Electrode materials designed for high electrochemical performance should exhibit high electrical conductivity and a large specific surface area with unique pore structures to access a significant amount of electrolyte ions at the electrode−electrolyte interface, subsequently supporting the electric double-layer capacitance. Among all of the nanomaterials, carbon materials such as graphene, carbon nanotubes, and carbon nanofibers[14] have found significance as promising electrode materials for electrochemical devices.

In today's world, there is a need to develop and scale up sustainable, clean energy sources, and the technologies related to these are acknowledged worldwide as an urgent priority. The appropriate way to address the global economic issues is to make use of biomass.[15−18] The use of biomass or biowaste materials is substantially less harmful to the environment; they are abundant, inexpensive, and also help in the reduction of fossil fuels. Till date, the physical (stream, CO_2) and chemical (KOH, NaOH, $ZnCl_2$) methods of activation of biomass/biowaste are the most commonly used methods to develop porous carbon nanomaterials with high surface areas and unique porosities.[19,20] It has been realized that the specific surface area and the pore structure of carbon materials are the two important features that can influence the rate capability and the specific capacitance of supercapacitors. This is because the capacitance of a supercapacitor commences from the electrostatic charge accumulation at the electrode−electrolyte interface. In recent times, porous carbon materials with two-dimensional (2D)[21] and three-dimensional (3D) microstructures[22] have found significance as promising electrode materials for electrochemical devices since they have better accessibility and can offer significant active surface area for electrolyte adsorption to various pore sizes and also reduce the diffusion length of electrolyte ions into micropores.[23] Therefore, extensive research methods including the use of expensive soft and hard templates and metallic and toxic chemically or physically active reagents to produce porous carbons have been developed. However, these routes still found some limitations due to the complex and multiple preparation steps and the need for expensive carbon precursors and expensive sacrificial templates,[24,25] and hence limiting their large-scale applications. Therefore, emerging inexpensive and nontoxic green approaches for the development of 2D and 3D porous carbons have become urgent.

Herein, a less expensive, novel, scalable, and single-step process is explored to develop nitrogen-doped porous carbon nanomaterials with three unique morphologies by utilizing three different parts of a single biowaste *Bombax malabaricum* as a carbon precursor. In this work, comparative analyses of three microstructures from *B. malabaricum* have been presented by studying their material properties and evaluating their supercapacitive performance.

These trees are commonly planted in African and Asian countries, and they can produce around 2000−4000 seeds at a time. In the spring season, *B. malabaricum* shells open up on the tree and a large number of loosely imbedded seeds and the pale yellow microfibers from the broken shell fly in the wind. *B. malabaricum* fibers can grow up to 0.3−1.25 in. long, with diameters of ∼30 to 36 μm, and they comprise both lignin and cellulose. The floss is light in weight compared to the normal cotton but is too firm for spinning. Earlier reports demonstrated that various types of biomass-based porous carbons have found potential applications as electrode materials for supercapacitor applications due to their ability to be carbonized, the specific inherent microstructures, and the presence of organic and inorganic elemental contents to form carbon nanomaterials. The various parts of *B. malabaricum* should have unique inherent microstructures. The examination of these microstructures and the electrochemical properties of the prepared carbon materials derived from them are beneficial to not only make use of biowaste but also understand the variance of microstructure formation based on their inherent structures and organic−inorganic elemental compositions, which help us in proper selection of biomass and development of high-performance supercapacitor electrode materials. Here-

DOI: 10.1021/acsomega.9b00263
ACS Omega 2019, 4, 6399−6410

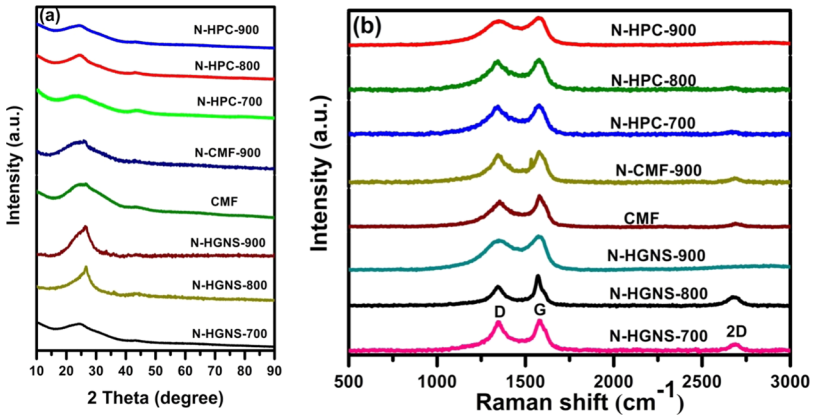

Figure 2. (a) X-ray diffraction patterns of N-HGNS-700−900, CMF, N-CMF, and N-HPC-700−900; (b) Raman spectra of N-HGNS-700−900, CMF, N-CMF, and N-HPC-700−900.

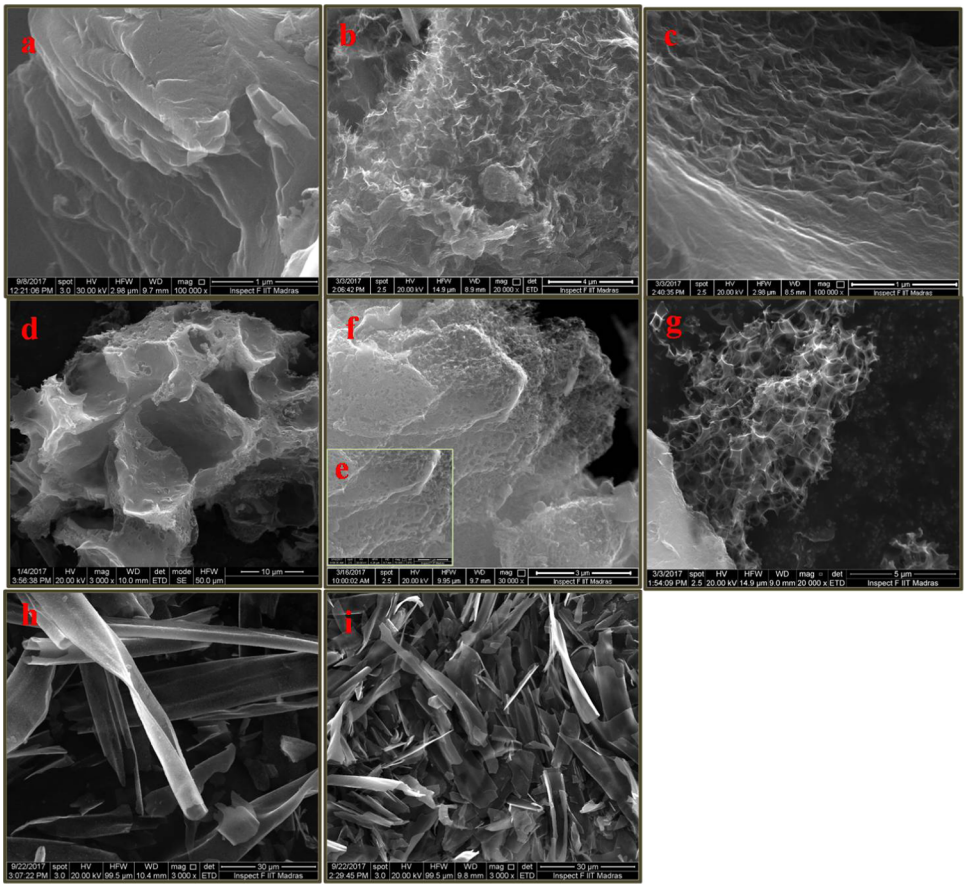

Figure 3. Scanning electron microscopy (FE-SEM) images of (a) N-HGNS-700, (b) N-HGNS-800, (c) N-HGNS-900, (d) N-HPC-700, (f) N-HPC-800 ((e) inset showing the low-magnified image), (g) N-HPC-900, (h) CMF, and (i) N-CMF-900.

in, we presented a range of carbon nanomaterials developed by a simple pyrolysis process in an inert atmosphere without using any toxic activation methods. The developed materials acquired high specific surface areas with unique hierarchical pore structures, moderate conductivity, and uniform nitrogen doping.

Typically, the supercapacitor device performance depends primarily on two factors: the electrode material and the electrolyte that we use. To verify the stable electrochemical performance of the prepared electrode materials in various electrolytes, these novel carbon materials are explored as electrode materials for supercapacitor applications with excellent electrochemical performance both in acidic and neutral aqueous electrolytes, and also we have demonstrated a fully biocompatible solid-state supercapacitor.

RESULTS AND DISCUSSION

Initially, three simultaneously N-doped unique microstructures are derived from three different parts of biowaste *B. malabaricum* and the developed samples are examined as active electrode materials for supercapacitor applications. The overall synthesis process is shown in schematic Figure 1. The

DOI: 10.1021/acsomega.9b00263
ACS Omega 2019, 4, 6399−6410

structural properties of as-synthesized N-HGNS, N-CMF, and N-HPC are characterized in detail, as shown in Figure 2a. The diffraction peaks located at around 26.3 and 43° in the X-ray diffraction (XRD) pattern indicate the presence of graphene nanosheets for N-HGNS, which shows a high graphitization degree, and these characteristic peaks are related to the (200) and (101) planes, which show a turbostratic graphitic structure. The XRD patterns of N-CMF suggest the graphitic nature of the carbon from the peaks at 25.9 and 43°. In the case of N-HPC-700 to N-HPC-900, the XRD pattern shows two diffraction peaks located at around 24.8 and 43°, revealing the low degree of graphitization, which can be ascribed to the (002) and (100) planes of the disordered carbon layers, respectively. The high intensity of the low-angle diffraction peak at 43° may be attributed to the presence of abundant micropores in N-HPC. The decrease in intensity of the 43° diffraction peak with an increase in temperature indicates the high graphitization level.

The graphitic nature is further verified by Raman spectroscopy. The characteristic Raman peaks of the three unique microstructures are located at around ∼1350 and 1580 cm^{-1} (D and G bands of carbon, respectively). The D band is associated with the defects and disorder present in the carbon nanomaterials, while the G band is associated with the graphitic level.[26,27] The I_D/I_G intensity ratio is used to evaluate the amount of graphitic ordering present in the carbon. For the N-HGNS, the I_D/I_G ratio reduces from 0.87 for N-HGNS-700 to 0.63 for N-HGNS-900, which specifies that a high amount of ordered carbon present in *B. malabaricum* is carbonized at high temperature. Specifically, as the carbonization temperature increases, the Raman spectra of the carbonized N-HGNS not only simply display the D and G bands but also show a peak at around 2689 cm^{-1}, which signifies the 2D band of graphene. In the Raman spectrum of HGNS-900, the 2D band (defining the number of graphene layers) is strong, which indicates that a large amount of graphene-like sheets exist in HGNS-900. Therefore, the resulted Raman characteristic peaks confirm that the carbonization process of the *B. malabaricum* shells significantly increases the graphitization level of the carbon nanomaterials. Figure 2b displays the Raman spectra of N-CMF samples before and after carbonization. The I_D/I_G intensity ratio of the N-CMF before carbonization (I_D/I_G = 0.81) exhibits a smaller change than that of the ratio after carbonization (I_D/I_G = 0.88), which specifies a higher graphitization degree of the carbonized N-CMF. Similarly, the intensity of the D band of the N-HPC is higher than that of the G band, which signifies a lower degree of graphitization present in the N-HPC. As explained before, the variation in the graphitization levels of N-HGNS, N-CMF, and N-HPC is probably ascribed to the variation in the inherent microstructures, the chemical composition of samples, and proper carbonization temperature and process. The presented organic and inorganic elemental compositions in the pristine *B. malabaricum* are listed in Table S1.

The morphologies of the as-synthesized carbon nanomaterials are characterized using scanning electron microscopy (SEM) and transmission electron microscopy (TEM). The inherent microstructures of *B. malabaricum* shells and seeds are shown in Figure S1. The SEM images of N-HGNS-700, N-HGNS-800, and N-HGNS-900 are shown in Figure 3a−c. The carbonization temperature also remarkably affects the morphology of the as-synthesized carbon materials. The carbonization process at 700 and 800 °C gives rise to partial separation of the graphitic layers. At 900 °C, it is significantly revealed that the microstructure consists of, specifically, wrinkled sheets in line with one another, with thick carbon layers at the edges, which tend to impart crystalline nature to N-HGNS-900. In comparison with typical carbon nanosheets, the thin and well-defined wrinkles are significant in the as-prepared graphene-like nanosheets, which could develop from the strong gasification during carbonization. In the carbonization process, several gas bubbles located between the multilayers contribute to the development of interconnected thin and wrinkled few-layered graphene-like nanosheets. The field emission scanning electron microscopy (FE-SEM) images of N-HPC-700 to N-HPC-900 are shown in Figure 3d,f,g, which obviously reveal that they have a distinctive three-dimensional honeycomb-like structure comprising various interconnected pores. The morphology of the as-prepared microfibers before and after the carbonization process is shown in Figure 3h, and we identified that all of the fibers are smooth, helically turned, and striped like a tube with an abrasive granular surface. After carbonization at 900 °C (Figure 3i) in the presence of $NaHCO_3$ and melamine, carbon microfibers are partially disintegrated. Hence, the simultaneously N-doped carbon microflakes are attained from these carbonized striplike tubes. Further structural information of N-HGNS-800 and N-HGNS-900 is provided with the high-resolution TEM (HR-TEM) images, as shown in Figure 4a,b. It confirms the

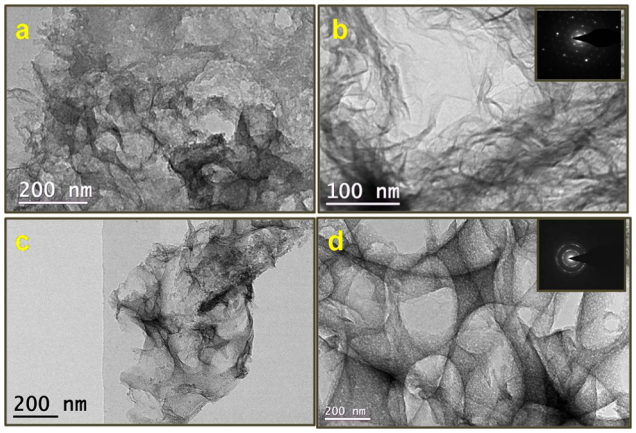

Figure 4. Transmission electron microscopy (FE-SEM) images of (a) N-HGNS-800, (b) N-HGNS-900 (inset shows the SAED pattern), (c) N-HPC-800, and (d) N-HPC-900 (inset shows the SAED pattern).

wrinkled sheetlike structure with various pores that can be clearly observed. The selected area electron diffraction (SAED) pattern of N-HGNS-900 signifies a well-defined diffraction ring pattern, which reveals the high degree of crystalline nature of the carbon walls. Similarly, for N-HPC-800 and N-HPC-900, the HR-TEM images, as shown in Figure 4c,d, reveal the honeycomb structure with numerous pores and the SAED pattern reveals the polycrystalline nature of the carbon wall.

To further examine the textural properties of the three different microstructured porous carbon nanomaterials, N_2 adsorption and desorption isotherm characteristics are studied for the samples at 77 K. As shown in Figure 5a, it is evident that N-HGNS-700 to N-HGNS-900 samples have both type-IV and type-I nitrogen adsorption−desorption isotherm characteristics, which signify the hierarchical porous (micro/meso/macropore) structures of the N-HGNS materials. There

DOI: 10.1021/acsomega.9b00263
ACS Omega 2019, 4, 6399−6410

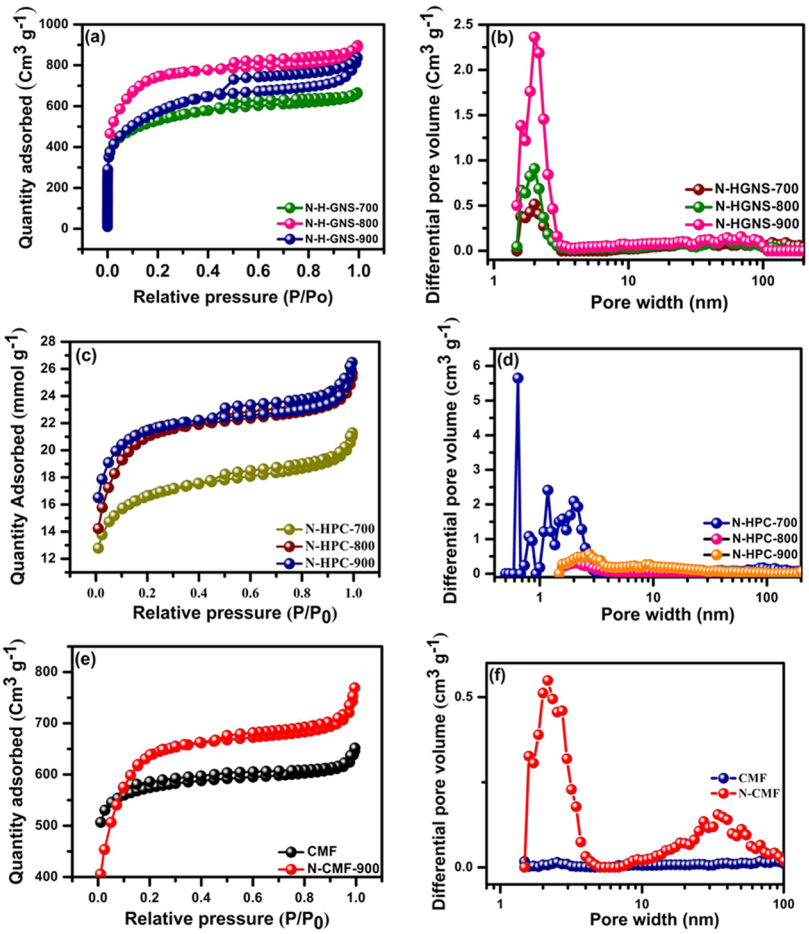

Figure 5. Nitrogen adsorption−desorption isotherms at 77 K: (a) N-HGNS-700−900, (c) N-HPC-700−900, and (e) N-CMF-900; pore size distributions of (b) N-HGNS-700−900, (d) N-HPC-700−900, and (f) N-CMF-900.

are substantial sharp rises at low pressures, signifying the presence of micropores, and a wide knee that enlarges from P/P_o = 0.01 to 0.45 for HGNS-700 to HGNS-900, signifying the presence of a large number of mesopores. However, a substantial hysteresis loop and noticeable edges at high pressure (P/P_o > 0.45) for N-HGNS materials signify the formation of a small number of macropores. Figure 5b shows the pore size distributions (PSDs) measured using the density functional theory model. The unique porous nature of N-HGNS can be attributed to the interaction between $NaHCO_3$ and *B. malabaricum*. This specific nanosheet structure of the carbonized shell reduces the diffusion length of electrolyte ions, resulting in excellent electrochemical properties of the N-HGNS. Similarly, N-HPC-700 to N-HPC-900 (Figure 5c) exhibit both type-I and type-IV absorption isotherms, indicating the presence of micro- and mesopores. From the PSD (Figure 5d), it is confirmed that there are numerous mesopores and a small amount of micro and mesopores presented in the N-HPC. The CMF (Figure 5e) shows the characteristic type-I isotherm with considerable adsorption at low pressure, which indicates the presence of micropores. After activation with $NaHCO_3$ at 900 °C, the obvious hysteresis loop exists at high pressures. Such a transition in the isotherm curves indicates the generation of mesopores after activation with $NaHCO_3$. Moreover, the H4-type characteristic loop in the N-CMF indicates the generation of slitlike pores. CMF shows the Brunauer−Emmett−Teller (BET) specific surface area of 392 $m^2\ g^{-1}$. After activation, the specific surface area of N-CMF increases to 1478 $m^2\ g^{-1}$. It is investigated that the simple carbonization of the raw *B. malabaricum* cotton stalk leads to the formation of micropores. Furthermore, activation with $NaHCO_3$ at 900 °C results in the transition of these micropores into meso- or even macropores. The above results prove that the carbonization process in the *B. malabaricum* using $NaHCO_3$ can produce carbon nanomaterials with a large specific surface area and unique hierarchical porous nature. It is also observed that the specific surface area and pore volume increase but the pore size reduces gradually with increasing temperature for all of the prepared materials. The analyzed BET surface area, pore size, and pore volumes of all of the as-prepared materials are listed in Table 1. The developed hierarchical pore structures with the prepared electrode material will benefit in enhancing the electrochemical performance. The macropores act as ion buffering reservoirs, mesopores reduce the ion diffusion length and act as ion transporting channels, and micropores can improve the ion and charge storage capacities.

The mechanism for the preparation of simultaneously N-doped high-surface-area wrinkled few-layered graphene nanosheets is elucidated below. *B. malabaricum* shells, $NaHCO_3$, and melamine are used as precursors, in which the *B. malabaricum* shell acts as a carbon source, $NaHCO_3$ acts as a pore-developing agent, and melamine acts as a N-doping source. While changing the pyrolysis temperature from 700 to 900 °C, high-surface-area porous N-HGNSs are produced. Moreover, through the reaction with the decomposed

DOI: 10.1021/acsomega.9b00263
ACS Omega 2019, 4, 6399−6410

Table 1. BET Surface Area and Pore Size Distribution of N-HGNS, N-HPC, and N-CMF

sample	BET surface area ($m^2\ g^{-1}$)	total pore volume ($cm^3\ g^{-1}$)	micropore volume ($cm^3\ g^{-1}$)	mesopore volume ($cm^3\ g^{-1}$)	pore width (nm)
N-HGNS-700	1727	1.21	0.51	0.70	4.64
N-HGNS-800	1944	1.31	0.57	0.77	4.63
N-HGNS-900	2402	1.81	0.64	1.19	3.60
N-HPC-700	1163	0.98	0.40	0.57	4.38
N-HPC-800	1485	1.27	0.53	0.72	4.74
N-HPC-900	2120	1.40	0.45	0.87	3.58
CMF	392	0.34	0.17	0.16	4.94
N-CMF-900	1478	1.18	0.42	0.70	4.00

ammonia (NH_3) from melamine, a fraction of carbon atoms are replaced by nitrogen. Finally, N-doped HGNSs are developed. In the present work, Na_2CO_3 played an important role in delaminating and utilizing the sp^3-hybridized carbon atoms between the graphitic layers of *B. malabaricum*-derived carbon. Once Na_2CO_3 is melted, the generation of sodium atoms catalyzed the graphitic microstructures to form a graphene nanosheet-like structure. In addition, the pore structures distinguished in the SEM images are created by the release of CO_2 from the surfaces once $NaHCO_3$ is decomposed. Then, sodium carbonate is evaporated and entrapped in the inner pores generated by CO_2 gas bubbling, which tends to contribute to the development of micro and mesopores. The generated CO_2 further reacts with carbon via gasification, resulting in thinner walls. As reported earlier, sodium and potassium are likely to catalyze the high graphitization of amorphous carbon, and these atoms can create charge transfer centers with aromatic hydrocarbons and also with graphite layers to obtain crystallinity. In addition to the above reasons for microstructure formation due to the carbonization process in the presence of Na_2CO_3, the inherent inorganic elements such as K, Na, P, and Cl^- also affect the self-activation of *B. malabaricum* shells. Here, Cl^- ions etch out the carbon structures and create micro- and mesopores and K and Na can prevent the development of van der Waals force, which overcomes the restacking of sp^2-hybridized carbon layers and develops a graphene-layered structure. Also, with an increase in the calcination temperature, oxygen participates in etching the carbon nanosheets to develop thin graphene layers. As we know, carbon reduces itself at a higher temperature (above 600 °C), developing a large number of micropores on carbon nanosheets. Restacking of carbon nanosheets can be avoided in a 3D interconnected honeycomb structure, and this 3D microstructure with a hierarchical pore structure can access the electrolyte ions by reducing the ion diffusion and transportation length.

The pore generation mechanism is explained as follows

$$2NaHCO_3 \rightarrow Na_2CO_3 + CO_2 + H_2O \quad (1)$$

$$Na_2CO_3 \rightarrow Na_2O + CO_2 \quad (2)$$

$$Na_2CO_3 + 2C \rightarrow 2Na + 3CO \quad (3)$$

$$Na_2O + C \rightarrow 2Na + CO \quad (4)$$

$$CO_2 + C \rightarrow 2CO \quad (5)$$

The presence of wrinkles provides an improved electrolyte reaction interface with the carbon nanosheets.

The oxygen functionalities on the surface of the precarbonized sample could help in the formation of three-dimensional hierarchical porous carbons. The precarbonized sample is initially mixed with $NaHCO_3$ and melamine, and $NaHCO_3$ decomposed to Na_2CO_3 during the carbonization process to produce sodium salts and then a molten mixture of sodium and biochar. At higher carbonization temperatures, these sodium salts and biochar start pyrolysis to form CO_2, H_2O, CO, and other gases; simultaneously, the molten mixture could expand like a sponge, which implicates the release of gases to form a hierarchical porous structure. Through the gas dissipation and pyrolysis of biochar, continuous interconnected 3D carbon walls with a hierarchical porous structure would develop. Therefore, the oxygen functionalities on the biochar surface are decomposed during the carbonization, leading to the formation of the molten mixture of sodium salt and biochar during the carbonization process.[28,29]

The carbon (C), nitrogen (N), and oxygen (O) contents of the prepared electrode materials are detected by X-ray photoelectron spectroscopy (XPS) analysis, and the corresponding elemental compositions are listed in Table 2. The high-resolution deconvoluted C 1s spectrum of N-HGNS-900 is shown in Figure S2. It shows an intense peak at around 284.5 eV, which is assigned to the sp^2 carbon (C═C) of graphene, and also shows a broad high-intensity shoulder peak, which results from C═N bonds (at 285.7 eV) and low-intensity sp^3 C−N bonds. The nitrogen content decreases slightly when the carbonization temperature is increased, while the O content increases slightly in this process. From these results, we can observe that both N and O contents can be controlled by properly adjusting the carbonization temperature. To understand the type of nitrogen species present on the surface of the carbon matrix, XPS analysis is performed to examine the chemical compositions of N-HGNS, N-HPC, and N-CMF. The high-resolution N 1s spectrum (Figure S3) is deconvoluted into four different component peaks, which are

Table 2. Chemical Compositions of Prepared Carbon Materials Determined by X-ray Photoelectron Microscopy

	XPS (atom %)			nitrogen functional groups (% concentration)			
	C	O	N	pyrrolic N	pyridinic N	quaternary N	oxidized N
N-HGNS-700	86.63	5.36	8.01	65.46	16.02	18.52	
N-HGNS-800	85.01	7.87	7.12	47.15	19.90	32.95	
N-HGNS-900	84.87	10.18	4.95	35.07	17.01	32.53	15.39
N-HPC-700	85.79	6.84	7.37	65.71	19.88	14.41	
N-HPC-800	84.01	9.27	6.72	64.80	10.13	25.07	
N-HPC-900	83.88	12.54	3.58	32.13	19.72	32.59	15.56
N-CMF-900	85.97	10.57	3.46	38.04	20.36	19.93	21.67

DOI: 10.1021/acsomega.9b00263
ACS Omega 2019, 4, 6399−6410

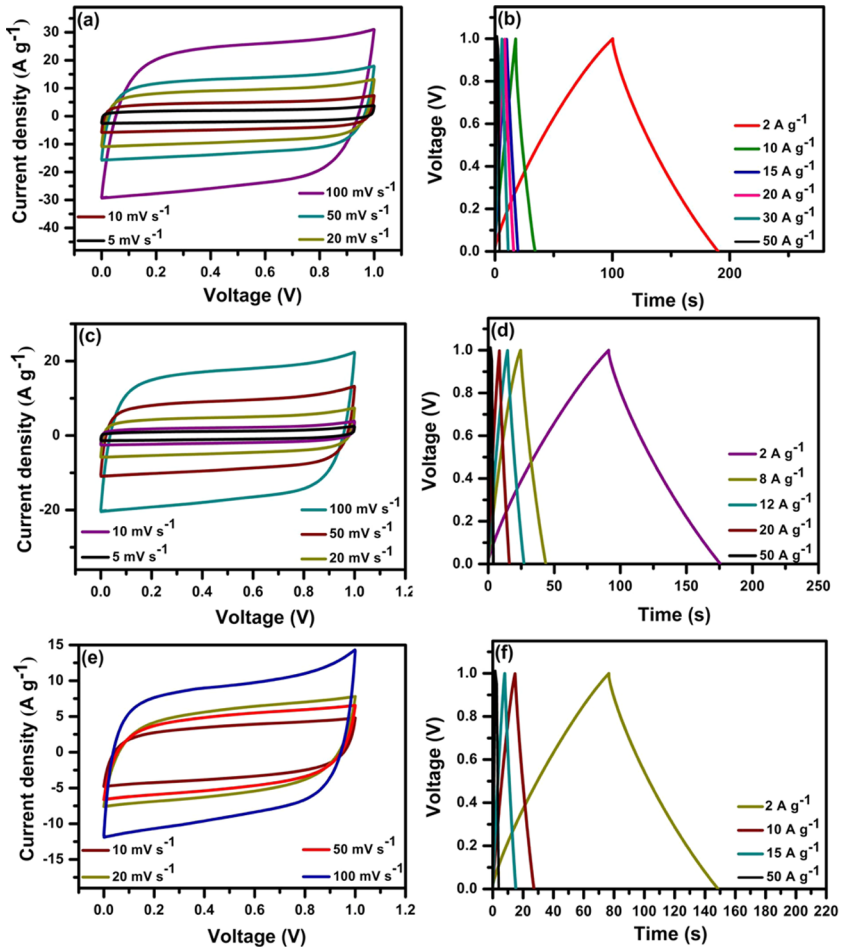

Figure 6. Electrochemical capacitive behavior of the electrode materials measured in a two-electrode system: (a) CV curves at various scan rates and (b) galvanostatic charge−discharge (GCD) curves at different current densities for N-HGNS-900; (c) CV curves and (d) GCD curves for N-HPC-900; and (e) CV curves and (f) GCD curves for N-CMF-900 in 1 M H_2SO_4 (calculations are based on the mass of the active material on the two electrodes).

attributed to pyrrolic (N5), pyridinic (N6), quaternary (NQ), and oxidized nitrogen (N-Ox). It is understood that with the increase of carbonization temperature the amount of N-5 and N-6 decreases, while the amount of N-Q and N-Ox increases. This signifies the conversion of pyrrolic N to pyridinic N, quaternary N, and oxidized N at high carbonization temperatures. This is because the pyrrolic N is thermally unstable and transforms gradually to pyridinic and quaternary N above 700 °C, while pyridinic N converts into quaternary and oxidized N above 800 °C during the carbonization process. This could be due to the higher thermal stability of quaternary N and oxidized N. In general, pyrrolic N and pyridinic N are situated along the wings of the graphitic carbon plane, while the quaternary N can be situated both at the edge and within the oxidized graphene layers.

The electrochemical performance of the prepared electrode materials is examined in three electrode configurations as shown in Figure S4, and the detailed description of electrochemical performance is presented in the Supporting Information.

To explore the electrochemical performance of as-prepared electrode materials, two-electrode symmetric supercapacitor devices are designed using 1 M H_2SO_4 as the electrolyte. From Figure 6a−c, it can be seen that all of the cyclic voltammetry (CV) profiles show a distinctive rectangular shape. N-HGNS shows a larger area under the CV curve than the N-HPC, demonstrating high charge transportation capability and ease of ion transport within the N-HGNS electrode material. As shown in Figure 6b,d,f, all of the charge−discharge profiles are linear and symmetric at various current densities. Also, there is no obvious *IR* drop presented for the N-HGNS, which denotes high columbic efficiency. The N-HGNS-900 sample exhibits high specific capacitances of 358.4, 330, 312, 304, 297, and 288 F g^{-1} at the current density range from 2 to 50 A g^{-1} with 80.3% rate capability. The specific capacitances of the N-HPC-based cell are 337.6, 304, 297.6, and 273.6 at 2 to 50 A g^{-1} with 81% rate capability.

To examine the electrical conductivity, the resistance, and the charge transportation process at the electrode/electrolyte interface, the electrochemical impedance spectroscopy technique is used in the frequency range from 0.01 Hz to 100 kHz, with the amplitude of 5 mV, and the corresponding Nyquist plots are shown in Figure S5. In the Nyquist plots, a small semicircle at high frequency and a vertical line at low frequency are noticed in all of the plots. The intercept of the semicircle along the x-axis in the high-frequency region corresponds to the series or solution resistance, which includes the ionic resistance of the electrolyte, the inherent resistance of the prepared electrode materials, and the contact resistance between the electrode/electrolyte interface and the current

DOI: 10.1021/acsomega.9b00263
ACS Omega 2019, 4, 6399−6410

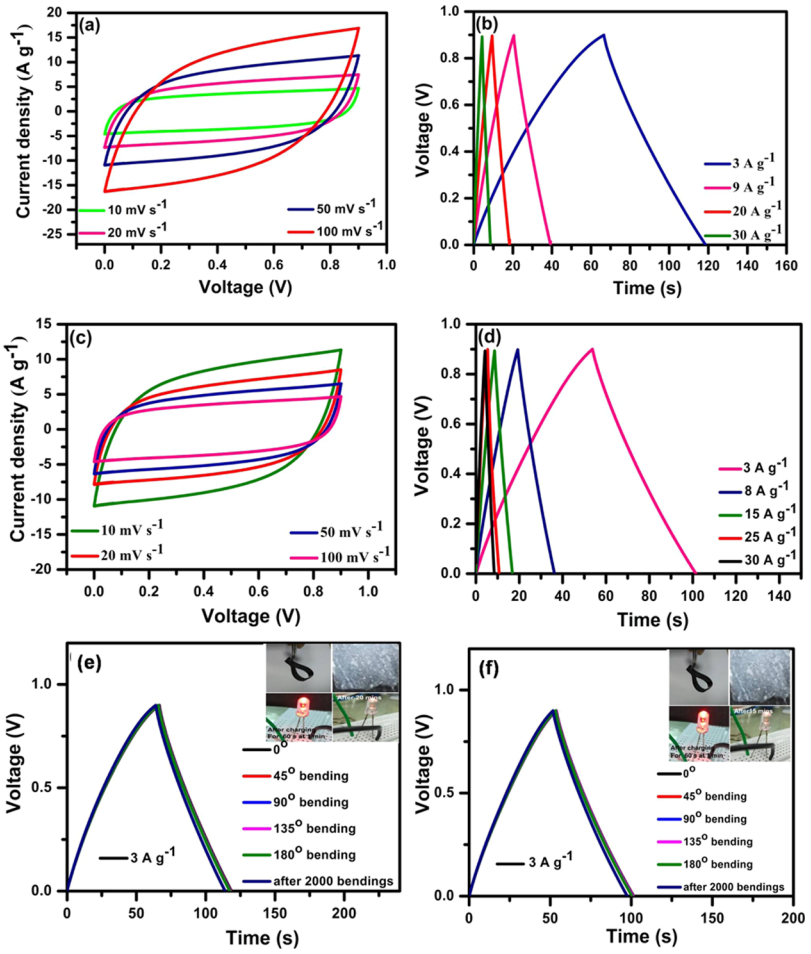

Figure 7. Electrochemical capacitive behavior in a solid-state flexible system: (a) CV curves at various scan rates for N-HGNS-900, (b) GCD curves at various current densities in a NaCl−agarose solid-state gel electrolyte for N-HGNS-900, (c) CV curves for N-HPC-900, (d) GCD curves in the NaCl−agarose solid-state gel electrolyte, (e) N-HGN-900 and (f) N-HPC-900 CD curves of a fully biocompatible flexible supercapacitor at different bending angles of 0, 45, 90, 135, and 180° and after 2000 cycles of bending, and (f) CD curves at a current density of 3 A g^{-1} (inset shows the fabrication of a flexible device and biodegradable hydrogel electrolyte).

collector. The equivalent series resistances (ESRs) of the as-prepared electrode materials are 0.68 Ω (N-HGNS-900), 0.74 Ω (N-HPC-900), and 0.7 Ω (N-CMF-900), which indicate that N-HGNS-900 has a lower series resistance with a well-behaved ion reaction at high frequency among all of the three electrode materials. In the case of an ideal supercapacitor electrode, both charge transfer resistance and series resistance should be low. After activation at 900 °C, all of the three prepared electrode materials show semicircles. The values of charge transfer resistance (R_{ct}) for N-HGNS-900, N-HPC-900, and N-CMF-900 are 0.04, 0.12, and 1.8 Ω, respectively. These resistance values support the charge−discharge data, which indicates that the N-HGNS and N-HPC electrodes exhibit the best electrochemical performance and the N-HGNSs have improved electrical conductivity and electrochemical performance than the N-HPC. It is noticed that the R_{ct} of the N-HGNS is much lower than that of the N-HPC and N-CMF. This might be due to the well-developed microstructure of N-HGNS with a small number of micro- and macropores and a significant number of mesopores with the pore size of around 3 nm. In addition, the wrinkled thinner walls of the N-HGNSs improve the diffusion of the electrolyte ions into the well-interconnected hierarchical pores. The slope of the 45° declined line in the mid-frequency range denotes the Warburg impedance, attributed to the frequency dependence of electrolyte ion diffusion/transfer in the electrolyte to the electrode surface. The vertical line in the low-frequency region is a characteristic of ideal capacitor behavior. Among all of the prepared electrode materials, N-HGNS-900 has the low ESR, smallest R_{ct}, very small Warburg portion, and a vertical line in the low-frequency region, implying the optimum charge storage performance with the electric double layer capacitor behavior. This might result in a high conductivity, a greater specific surface area, and a well-interconnected hierarchical pore structure.

The detailed electrochemical behavior of N-HGNS and N-HPC in the neutral electrolyte, as shown in Figure S6, is presented in the Supporting Information.

Although solid-state polymer-based gel electrolytes show significant advances in the fabrication of flexible supercapacitor designs, they are finding practical limitations due to their expensive preparation methods and the effect of these on the environment because of the use of toxic chemicals. Herein, we present a simple, fully biocompatible solid-state gel-based supercapacitor device assembly using a NaCl−agarose hydrogel electrolyte. Agarose hydrogel is a low-cost material, which is biocompatible and contains a chemically interconnected agarose backbone with micrometer pores. Due to the

DOI: 10.1021/acsomega.9b00263
ACS Omega 2019, 4, 6399−6410

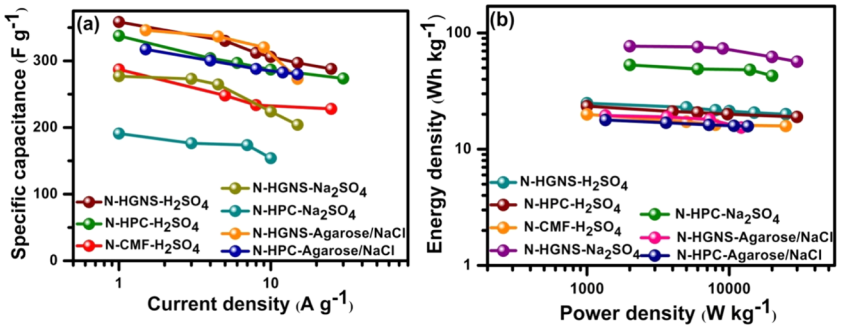

Figure 8. (a) Specific capacitances as a function of current densities in different electrolytes for N-HGNS-900 and N-HPC-900. (b) Ragone plot (plot of energy density vs power density) of various electrolytes for N-HGNS-900, N-HPC-900, and N-CMF.

interconnected pore structure and more water content, the agarose hydrogel is a bendable and environmentally friendly solid-state gel electrolyte with high ion mobility. The NaCl−agarose gel is prepared by inclusion of both Na^+ and Cl^- ions into the hydrogen-bonded interconnected self-assembly of molecules of agarose gel. This agarose gel promotes the rapid ion transfer channels, resulting in high storage capacity. It is recommended that the agarose hydrogel present an appropriate and environmentally friendly process for the stable, flexible supercapacitor market with improved capacitive performance. Figure 7a,c shows the CV curves for the N-HGNS and N-HPC in the NaCl−agarose hydrogel. It shows a rectangular shape at a scan rate ranging from 5 to 100 mV s^{-1} in the 0−0.9 V voltage window. Furthermore, the GCD curves (Figure 7b,d) of the assembled solid-state symmetric system with the NaCl−agarose hydrogel are studied at various current densities in the range of 3−30 A g^{-1}. The specific capacitances obtained from the charge−discharge curves for N-HGNS and N-HPC in the NaCl−agarose hydrogel are 345 and 317.3 F g^{-1} at 3 A g^{-1}, and specific capacitances of 273 and 280 F g^{-1} are still maintained at a high current density of 30 A g^{-1}. The assembled stable solid-state gel-based fully biocompatible supercapacitor device also exhibits high rate capability of 88% at a current density of 30 A g^{-1}, exhibiting an energy density of 19.4 Wh kg^{-1} at a power density of 1.3 kW kg^{-1}. There are no considerable changes observed in the CD curves when bending the flexible capacitor at angles from 0 to 180° at a current density of 3 A g^{-1}, as shown in Figure 7e,f for N-HGNS and N-HPC. The three flexible supercapacitors connected in series can power a red light-emitting diode for 20 and 15 min after charging for 60 s for N-HGNS and N-HPC, respectively.

It is well recognized that excellent cycle stability and high energy and power densities are needed for practical supercapacitor applications. Figure 8a,b shows the rate capability and the Ragone plots of the as-prepared electrode materials. All of the prepared electrode materials show more than 80% rate capabilities even at very high current densities. Compared with the other two N-HPC and N-CMF materials, N-HGNS shows high energy and power densities in all acidic and neutral aqueous electrolytes and also in solid-state gel electrolyte medium. The fabricated symmetric systems of the N-HGNS-900 and N-HPC-900 samples show higher energy densities of 24.8 and 23 Wh kg^{-1} at power densities of 1 kW kg^{-1} and 998 W kg^{-1}, respectively, in 1 M H_2SO_4; excellent energy densities of 76.94 and 53.05 Wh kg^{-1} at power densities of 2 and 1.8 kW kg^{-1}, respectively, in 0.5 M Na_2SO_4; and high energy densities of 19.46 and 17.84 Wh kg^{-1}, respectively, at power densities of 1.4 and 1.3 kW kg^{-1} in NaCl−agarose electrolytes. The energy densities of the N-HGNS and N-HPC samples are larger than those of earlier reported biowaste-based symmetric electrochemical devices, such as waste coffee beans (10−5.9 Wh kg^{-1}), petroleum coke waste (10−8 Wh kg^{-1}), and sunflower seed shell (6−3 Wh kg^{-1}). It can be seen that the N-HGNS, N-HPC, and N-CMF show excellent cycle stability (Figure S7) with capacitance retention of 96, 94.8, and 92.4% even after 10 000 cycles at 5 A g^{-1} current density, respectively. Here, N-HGNS shows more cycle stability compared to that of the other two electrode materials, which is because the N-HGNS electrode material has a well-developed pore structure and is stable throughout the cycle process. Also, the relatively high level of nitrogen functionalities also offers significant stability to the specific capacitance. The prepared electrode materials show excellent supercapacitive performance compared to the recent reports, and the comparative results with the recent reports are listed in Table S2.

It is well reported that incorporation of even a small amount of nitrogen atoms can greatly enhance the physicochemical properties of the carbon matrix, such as electrochemical activity, conductivity, and oxidation stability. In both alkaline and acidic electrolyte media, it is believed that both pyrrolic N and pyridinic N are electrochemically active, which contributes to the additional pseudocapacitance, whereas the incorporated quaternary N into the graphitic plane bonded to the three carbon atoms can be responsible for electron transfer and substantially improve the electrical conductivity of the carbon matrix. From these studies, we can assume that the incorporation of nitrogen atoms can greatly enhance electrochemical performance and rate capability.

Finally, in the case of N-HGNS, the improved electrochemical performance could be due to the nitrogen lone pair electrons, which offer more negative charges to the graphene π-system and therefore responsible for an improved conducting nature in addition to strong interaction with electrolyte ions. However, the incorporation of a higher amount of nitrogen alone is not always responsible for enhanced electrochemical performance, which also significantly depends on unique structural, morphological, and textural properties of the prepared electrode material. By considering the above results, the following characteristics may support such high electrochemical performance of the as-synthesized materials. Initially, the high specific surface areas with unique pore structures are beneficial for electrolyte interaction and build-up of electrolyte ions and therefore improve the charge storage capacity. Also, during the charging and discharging processes, the developed 2D and 3D microstructures of N-HGNS, N-CMFs, and N-

DOI: 10.1021/acsomega.9b00263
ACS Omega 2019, 4, 6399−6410

HPC may minimize the transfer length of electrolyte ions inside the micropores with the help of interconnected mesopores and result in excellent rate capability and long cycle life. Furthermore, electrolyte ions can easily diffuse through the 2D layered and honeycomb-structured carbon walls and be accessible to the micropores and hence substantially reducing the electrolyte ion transfer resistance. Finally, nitrogen doping can improve the wettability of carbon walls and electrical conductivity.[30] From these, we can conclude that the existing excellent synergy among high specific surface area, hierarchical porous structure, high conductivity, and improved electrochemical properties of carbon by N-doping contributes to pseudocapacitance and that a unique graphene sheet structure, which reduces the ion diffusion path length and charge transportation channel distance of N-HGNS, contributes to the excellent electrochemical performance. The synthesis process used here had the benefits of being novel, inexpensive, and feasible to develop on a large scale.

CONCLUSIONS

In conclusion, we used three different parts of a single biowaste with a unique inherent microstructure and composition to develop high-surface-area, conductive, and hierarchical porous-structured N-HGNS, N-HPC, and N-CMF nanomaterials through simple carbonization and self-activation processes from biowaste *B. malabaricum*. A comparative study of these three microstructures and of the impact of material properties on the electrochemical performance is performed. The stability of the electrode performance in various electrolytes is investigated in detail. N-HGNS-900 exhibits high electrochemical performance compared to the other two microstructures. The typical reason for these three unique microstructures is that the inherent organic elemental content (C, N) and the inorganic ion content (K, Na, P, or Cl^-) are different in the three parts. The high content of C and the internal inorganic elemental composition (such as K, Cl^-, and Na) influence self-activation. In addition, the carbonization process in the presence of Na_2CO_3 produces unique porous wrinkled graphene-like microstructures of the shell-derived carbon, which along with N-doping result in high conductivity and fast electrochemical kinetics. Moreover, all of the prepared electrode materials exhibit higher electrochemical performance compared to the earlier reports. The main features of the prepared electrode materials that influence the electrochemical performance are the high specific surface area, the unique hierarchical porous structure that provides excellent electrochemical interaction at the electrode and electrolyte interface and high-level graphitization, and high conductivity along with nitrogen doping. The obtained results demonstrate the probability of using nature for the development of electrode materials with high performance through simple methods.

EXPERIMENTAL PROCEDURE

N-Doped Wrinkled Few-Layered Graphene Nanosheets (N-HGNSs). The synthesis for graphene nanosheets follows multiple preparation steps, but herein, a simple and environmentally friendly synthesis method is presented to develop N-HGNS using naturally available *B. malabaricum* shells as the carbon source without using any templates or toxic and corrosive chemical activating agents. *B. malabaricum* shells have a unique inherent microstructure, with organic and inorganic composition that substantially differs from that of other biosources. The collected shells are dried at 70 °C in a microwave oven for 15 min and ground to a fine powder. The obtained fine powder (1 g) is mixed with $NaHCO_3$ (1 g) and melamine (150 mg), followed by carbonization at 700−900 °C under an inert argon (Ar) gas atmosphere. The resultant carbonized materials are washed thoroughly with ethanol and deionized (DI) water to remove any unwanted impurities and then dried. The resultant samples are named N-HGNS-700, N-HGNS-800, and N-HGNS-900 on the basis of different carbonization temperatures used.

Synthesis of N-Doped Carbon Microflakes (N-CMFs). The separated 1 g of *B. malabaricum* cotton stalk and 50 mL of 1 M H_2SO_4 are placed in a 150 mL Teflon-lined stainless steel autoclave. The sealed autoclave is heated at 180 °C for 12 h and then cooled down to room temperature. The resultant dark brown hydrochar is collected by washing with DI water and dried overnight at 70 °C. The dried hydrochar, $NaHCO_3$, and 15 wt % melamine are carbonized at 900 °C for 2 h under an Ar atmosphere, and the resultant sample is named N-CMF-900. For comparison, carbon fibers have been prepared by simply carbonization at 900 °C and named CMF.

Honeycomb-Structured Hierarchical Porous Carbon (N-HPC). In a typical synthesis method, the collected *B. malabaricum* seeds are dried in air and ground to a powder form. The dried powder is precarbonized at 300 °C for 2 h under Ar gas flow in a tubular furnace. The precarbonized material is ultrasonically mixed with $NaHCO_3$ and melamine in a 1:1:0.15 weight ratio. The above solution is kept undisturbed overnight. The solution is dried later, and the dried sample is placed in a tubular furnace and heated from 700 to 900 °C (heating rate, 5 °C min^{-1}) for 2 h, under the inert atmosphere. The sample is washed simultaneously with ethanol and DI water to remove the impurities such as Na_2CO_3. Finally, the sample is obtained by drying at 80 °C overnight in the oven and named N-HPC.

Characterization Techniques. The prepared material structural properties are examined using X-ray diffraction (XRD) analyses performed with a PANalytical X'Pert Pro X-ray diffractometer with Cu Kα (λ = 0.15406 nm) in the 2θ range from 5 and 90°. Raman characteristic peaks have been recorded using a confocal WiTech Raman spectrometer with a Nd:YAG laser (532 nm). For morphological studies, an FEI Inspect F scanning electron microscope and transmission electron microscopy (HR-TEM) with Tecnai G2 20 operated at 200 keV are used. The surface chemical compositions are examined by energy dispersive spectroscopy and X-ray photoelectron spectroscopy carried out using a Specs X-ray photoelectron spectrometer, X-ray source Mg Kα, and analyzer PHOIBOS 100MCD. Surface area and pore size distribution measurements are performed in a micrometrics ASAP 2020 instrument.

Electrochemical Measurements. The as-synthesized materials N-HGNS-900, N-CMF-900, and N-HPC-900 are ground with conductive carbon black and poly(tetrafluoroethylene) (85:10:5) by adding *N*-methyl pyrrolidinone to form a thick slurry. For the three-electrode system, the slurry is coated on a carbon paper with an area of 1 cm^2 × 1 cm^2 and a mass loading of ∼2 mg and used as a working electrode, a Hg/HgO wire as a reference, and Pt as a counter electrode. For the two-electrode system, the slurry is coated on carbon sheets. Then, two symmetric working electrodes are assembled with a polypropylene sheet as a separator dipped in

DOI: 10.1021/acsomega.9b00263
ACS Omega 2019, 4, 6399−6410

the electrolyte. These two electrodes are sandwiched between two Perspex sheets along with the stainless steel current collectors. The NaCl−agarose solid-state gel is prepared by mixing of 1 g of agarose powder with 0.5 M NaCl under continuous stirring and heating at 90 °C. The prepared semisolid gel is dropped onto a glass substrate and left to dry; after 1 h, a thick hydrogel film is separated from the glass substrate and sandwiched between the two N-HGNS and N-HPC electrodes while fabricating the supercapacitor full cell system. Electrochemical studies have been performed on a Biologic electrochemical workstation. The specific capacitance (C_p), power density (P), and energy density (E) values are calculated using the following equations.

$$C = \frac{I}{m \times \frac{\Delta E}{\Delta t}} \text{ for three electrode configuration} \quad (6)$$

$$C_s = \frac{I}{M \times \frac{\Delta E}{\Delta t}} \text{ for two electrode configuration} \quad (7)$$

$$E = \frac{1 \times C_s \times (\Delta E)^2}{2 \times 3.6} \quad (8)$$

$$P = \frac{E \times 3600}{\Delta t} \quad (9)$$

where C and C_s stand for the specific capacitance in three- and two-electrode systems, respectively. I is the discharge current, ΔE is the working potential or voltage of the electrode material, Δt is the discharge time, m is the mass of the active material on electrodes, M is the total active mass of the two electrodes, E is the energy density, and P is the power density by considering the mass of two electrodes.

■ ASSOCIATED CONTENT

Supporting Information

The Supporting Information is available free of charge on the ACS Publications website at DOI: 10.1021/acsomega.9b00263.

SEM images, XPS spectra, electrochemical studies, detailed performance notes; electrochemical impedance spectra; cycle stability plot; elemental composition; comparative results with earlier electrochemical reports; references (PDF)

■ AUTHOR INFORMATION

ORCID

Ramaprabhu Sundara: 0000-0002-7960-9470

Notes

The authors declare no competing financial interest.

■ ACKNOWLEDGMENTS

The authors thank the Indian Institute of Technology Madras (IITM), India, and the Ministry of Human Resources and Development, Government of India. One of the authors thanks the Department of Science and Technology (DST) for the financial support to establish Nano Functional Materials Technology Centre (NFMTC) through the SR/NM/NAT/02-2005 project.

■ REFERENCES

(1) Simon, P.; Gogotsi, Y. Materials for Electrochemical Capacitors. *Nanosci. Technol.* **2009**, 320−329.

(2) Sevilla, M.; Mokaya, R. Energy Storage Applications of Activated Carbons: Supercapacitors and Hydrogen Storage. *Energy Environ. Sci.* **2014**, *7*, 1250−1280.

(3) González, A.; Goikolea, E.; Barrena, J. A.; Mysyk, R. Review on Supercapacitors: Technologies and Materials. *Renewable Sustainable Energy Rev.* **2016**, *58*, 1189−1206.

(4) Qie, L.; Chen, W.; Xu, H.; Xiong, X.; Jiang, Y.; Zou, F.; Hu, X.; Xin, Y.; Zhang, Z.; Huang, Y. Synthesis of Functionalized 3D Hierarchical Porous Carbon for High-Performance Supercapacitors. *Energy Environ. Sci.* **2013**, *6*, 2497.

(5) Wang, Y.; Song, Y.; Xia, Y. Electrochemical Capacitors: Mechanism, Materials, Systems, Characterization and Applications. *Chem. Soc. Rev.* **2016**, *45*, 5925−5950.

(6) Gao, Z.; Zhang, Y.; Song, N.; Li, X. Biomass-Derived Renewable Carbon Materials for Electrochemical Energy Storage. *Mater. Res. Lett.* **2017**, *5*, 69−88.

(7) Mangisetti, S. R.; Pari, B.; Kamaraj, M.; Ramaprabhu, S. Performance of Partially Exfoliated Nitrogen-Doped Carbon Nanotubes Wrapped with Hierarchical Porous Carbon in Electrolytes. *ChemSusChem* **2018**, *11*, 1664−1677.

(8) Liu, L.; Niu, Z.; Chen, J. Unconventional Supercapacitors from Nanocarbon-Based Electrode Materials to Device Configurations. *Chem. Soc. Rev.* **2016**, *45*, 4340−4363.

(9) Liang, Y.; Zhang, W.; Wu, D.; Ni, Q. Q.; Zhang, M. Q. Interface Engineering of Carbon-Based Nanocomposites for Advanced Electrochemical Energy Storage. *Adv. Mater. Interfaces* **2018**, *5*, No. 1800430.

(10) Zheng, X.; Luo, J.; Lv, W.; Wang, D. W.; Yang, Q. H. Two-Dimensional Porous Carbon: Synthesis and Ion-Transport Properties. *Adv. Mater.* **2015**, *27*, 5388−5395.

(11) Wang, Y.; Dou, H.; Ding, B.; Wang, J.; Chang, Z.; Xu, Y.; Hao, X. Nanospace-Con Fi Ned Synthesis of Oriented Porous Carbon Nanosheets for High-Performance Electrical Double Layer Capacitors. *J. Mater. Chem. A* **2016**, *4*, 16879−16885.

(12) Zhu, Y.; Murali, S.; Stoller, M. D.; Ganesh, K. J.; Cai, W.; Ferreira, P. J.; Pirkle, A.; Wallace, R. M.; Cychosz, K. A.; Thommes, M.; et al. Carbon-Based Supercapacitors Produced by Activation of Graphene. *Science* **2011**, *332*, 1537−1542.

(13) Hou, J.; Cao, C.; Idrees, F.; Ma, X. Hierarchical Porous Nitrogen-Doped Carbon Nanosheets Derived from Silk for Ultrahigh-Capacity Battery Anodes and Supercapacitors. *ACS Nano* **2015**, *9*, 2556−2564.

(14) Frackowiak, E.; Beguin, F. Carbon Materials for the Electrochemical Storage of Energy in Capacitors. *J. Carbon* **2001**, *39*, 937−950.

(15) Shen, H.; Liu, E.; Xiang, X.; Huang, Z.; Tian, Y.; Wu, Y.; Wu, Z.; Xie, H. A Novel Activated Carbon for Supercapacitors. *Mater. Res. Bull.* **2012**, *47*, 662−666.

(16) Wang, H.; Yuan, H.; Sae Hong, S.; Li, Y.; Cui, Y. Physical and Chemical Tuning of Two-Dimensional Transition Metal Dichalcogenides. *Chem. Soc. Rev.* **2015**, *44*, 2664−2680.

(17) Yahya, M. A.; Al-Qodah, Z.; Ngah, C. W. Z. Agricultural Bio-Waste Materials as Potential Sustainable Precursors Used for Activated Carbon Production: A Review. *Renewable Sustainable Energy Rev.* **2015**, *46*, 218−235.

(18) Dutta, S.; Bhaumik, A.; Wu, K. C. W. Hierarchically Porous Carbon Derived from Polymers and Biomass: Effect of Interconnected Pores on Energy Applications. *Energy Environ. Sci.* **2014**, *7*, 3574−3592.

(19) Dutta, S.; Bhaumik, A.; Wu, K. C.-W. Hierarchically Porous Carbon Derived from Polymers and Biomass: Effect of Interconnected Pores on Energy Applications. *Energy Environ. Sci.* **2014**, *7*, 3574−3592.

(20) Enock, T. K.; King'ondu, C. K.; Pogrebnoi, A.; Jande, Y. A. C. Status of Biomass Derived Carbon Materials for Supercapacitor Application. *Int. J. Electrochem.* **2017**, *2017*, 1−14.

DOI: 10.1021/acsomega.9b00263
ACS Omega 2019, 4, 6399−6410

(21) Yu, X.; Zhao, J.; Lv, R.; Liang, Q.; Zhan, C.; Bai, Y.; Huang, Z.-H.; Shen, W.; Kang, F. Facile Synthesis of Nitrogen-Doped Carbon Nanosheets with Hierarchical Porosity for High Performance Supercapacitors and Lithium−sulfur Batteries. *J. Mater. Chem. A* **2015**, *3*, 18400−18405.
(22) Wang, D. W.; Li, F.; Liu, M.; Lu, G. Q.; Cheng, H. M. 3D Aperiodic Hierarchical Porous Graphitic Carbon Material for High-Rate Electrochemical Capacitive Energy Storage. *Angew. Chem., Int. Ed.* **2008**, *47*, 373−376.
(23) Kondrat, S.; Pérez, C. R.; Presser, V.; Gogotsi, Y.; Kornyshev, A. A. Effect of Pore Size and Its Dispersity on the Energy Storage in Nanoporous Supercapacitors. *Energy Environ. Sci.* **2012**, *5*, 6474.
(24) Li, Y.; Li, Z.; Shen, P. K. Simultaneous Formation of Ultrahigh Surface Area and Three-Dimensional Hierarchical Porous Graphene-like Networks for Fast and Highly Stable Supercapacitors. *Adv. Mater.* **2013**, *25*, 2474−2480.
(25) Chen, Z.; Wen, J.; Yan, C.; Rice, L.; Sohn, H.; Shen, M.; Cai, M.; Dunn, B.; Lu, Y. High-Performance Supercapacitors Based on Hierarchically Porous Graphite Particles. *Adv. Energy Mater.* **2011**, *1*, 551−556.
(26) Hao, G. P.; Lu, A. H.; Dong, W.; Jin, Z. Y.; Zhang, X. Q.; Zhang, J. T.; Li, W. C. Sandwich-Type Microporous Carbon Nanosheets for Enhanced Supercapacitor Performance. *Adv. Energy Mater.* **2013**, *3*, 1421−1427.
(27) Pimenta, M. A.; Dresselhaus, G.; Dresselhaus, M. S.; Cançado, L. G.; Jorio, A.; Saito, R. Studying Disorder in Graphite-Based Systems by Raman Spectroscopy. *Phys. Chem. Chem. Phys.* **2007**, *9*, 1276−1290.
(28) Song, S.; Ma, F.; Wu, G.; Ma, D.; Geng, W.; Wan, J. Facile Self-Templating Large Scale Preparation of Biomass-Derived 3D Hierarchical Porous Carbon for Advanced Supercapacitors. *J. Mater. Chem. A* **2015**, *3*, 18154−18162.
(29) Song, M.; Zhou, Y.; Ren, X.; Wan, J.; Du, Y.; Wu, G.; Ma, F. Biowaste-Based Porous Carbon for Supercapacitor: The Influence of Preparation Processes on Structure and Performance. *J. Colloid Interface Sci.* **2019**, *535*, 276−286.
(30) Hao, L.; Li, X.; Zhi, L. Carbonaceous Electrode Materials for Supercapacitors. *Adv. Mater.* **2013**, *25*, 3899−3904.

DOI: 10.1021/acsomega.9b00263
ACS Omega 2019, 4, 6399−6410